Large-Area Carbon Nanotube-Based Flexible

Composites for Ultra-Wide Range Pressure Sensing and Spatial Pressure Mapping

Hongbo Dai¹ and Erik T. Thostenson^{1,2,3*}

¹Center for Composite Materials, ²Department of Mechanical Engineering, and ³Department of Materials Science and Engineering, University of Delaware, Newark, Delaware 19716, United States

ABSTRACT: Flexible pressure sensors are of broad interest for applications including human-machine interfaces, wearable electronics, and object/motion detection. However, complexities associated with constituent materials, fabrication processes, sensing mechanisms and hardwiring, often hinder the large-scale applications of using high performance pressure sensors reported in the literature. Here we demonstrate a large-area, highly flexible and conformable, and mechanically robust pressure sensor using a silicone elastomer with an embedded nonwoven textile carrier coated with carbon nanotubes. The selected silicone polymer allows throughthickness deformability of the sensor while the high modulus textile carrier ensures in-plane stiffness and stability. The sensor has an initial electrical conductivity of 4.4 ± 0.38 S/m and is fabricated using a straightforward dip coating and polymer infusion process and can be easily scaled-up for large-scale applications. Based on its hierarchical composite structure, this piezoresistive pressure sensor possesses extremely high resilience under compression, a repeatable monotonic positive pressure correlation, and an ultra-wide elastic working range (5.5

 \pm 0.5 MPa) that can be segmentally linearized. A true two-dimensional modality for spatial pressure mapping is realized by utilizing electrical impedance tomography (EIT) and demonstrated to yield conductivity maps that can estimate the location, shape and amplitude of both localized and distributed pressure with simple contact areas.

KEYWORDS: Flexible composite, carbon nanotube, nonwoven fabric, ultra-wide range pressure sensing, electrical impedance tomography, spatial pressure mapping

1. INTRODUCTION

Pressure sensors transform compressive stimuli into electrical signals.¹ Over the past decade, tremendous research has been devoted to development of flexible pressure sensors owing for a wide range of applications, including object/motion detection,² wearable electronics,^{3,4} human-machine interfaces,⁵ and robotics.⁶ To date, numerous flexible pressure sensors have been reported in literature typically as combinations of sensing elements on flexible substrate materials based on the four major sensing mechanisms of capacitance,⁷⁻¹⁰ piezoelectricity,^{11,12} piezoresistivity,¹³⁻²² and triboelectricity.^{23,24} Among them, piezoresistive pressure sensors have been extensively studied due to their simple structures and straightforward sensing mechanism where the sensor signal results directly from the resistance change of conductive elements and their networks in reaction to external stimuli.¹ The active sensing elements are commonly formed by the metallic nanowires ⁶ and particles,¹ conductive polymers,^{4,6} and carbon-based structures.^{3,4} Particularly, carbon nanotubes (CNTs) can easily establish piezoresistive networks at a low weight concentration due to their high aspect ratio (length/diameter), outstanding electrical properties,³ and easy availability.²⁵ Currently, the market price for the multi-walled CNTs is on

the order of one US dollar per gram, which is significantly lower than the commercial graphenebased nanomaterials and silver nanowires (see Table S1 in supporting information).

However, the performance of CNT-based flexible pressure sensors with respect to sensitivity, working range, response and recovery time, and stability are largely scattered in literature due to complicated treatments to both CNTs and substrates and diverse processing methods. 14-17,20,21 For example, Park et al. 14 recently reported an extremely sensitive pressure sensor, which has a size of 1 cm², based on a microdome-structured polydimethylsiloxane (PDMS) with a CNT coating that exhibited a varying sensitivity of 4.7-3.0×10⁴ kPa⁻¹ in the working range of 0-26 kPa. Jian and co-workers ¹⁷ fabricated a 1.5×1.5 cm² pressure senor with an aligned CNT/graphene hybrid film and bionically microstructured PDMS that showed an ultralow detection limit of 0.6 Pa, a pressure-dependent sensitivity of 19.8-0.27 kPa⁻¹, and high stability for over 35,000 cycles, but the sensor has a very narrow working range (< 6 kPa). Liu et al. 15 utilized a dip-coating process to coat single-walled CNTs onto braided cotton fabric and made a 0.45×0.45 cm² all-textile sensor that presented a sensitivity of 14.4 kPa⁻¹ and working range up to 20 kPa. Chen and coworkers ¹⁶ coated CNTs onto polyurethane sponge strips, aligned them orthogonally and then infused the assembly with PDMS to obtain a cross sensor (3 cm in diameter) able to distinguish both normal pressure and bending.

CNT-based flexible pressure sensors capable of detecting pressure in the MPa-range have been very rarely reported. ¹⁻³ Recently, Doshi and Thostenson ²⁶ fabricated a CNT-based fabric sensor using an electrophoretic deposition approach. This sensor has an ultra-wide dynamic sensing range from tactile pressures (<10 kPa) up to 40 MPa with an average sensitivity of 0.05 MPa⁻¹. ²⁶ In comparison, a few flexible sensors with ultra-wide working range have been developed with pizeotronic transistors (PTs), for example, a 2D ZnO nanoplatelet-based PT with

the working range of 0-3.64 MPa by Liu *et al.*²⁷ and a patterned ZnO nanowire/p-Polymer-based PT with 40-100 MPa working range by Bao *et al.*²⁸ Recently, Wu and co-workers²⁹ introduced a sandwich sensor based on PDMS and vertical graphene nanosheets that are both ultra-sensitive and stretchable. The sensitivity to pressure varied with graphene nanosheet height and was estimated to be \sim 0.030, 0.014, and 0.002 kPa⁻¹ for heights of 13, 7, and 2 µm thick, respectively, at pressures up to 500 kPa.

In addition to basic pressure detection, the capability of spatial pressure mapping is highly desirable for advanced large-area flexible pressure sensors, 3,5 especially for applications in human-machine interface. Currently, sensing arrays and networks consisting of point-type sensors have been largely adopted to cover a surface area and map the resolved pressure information from grid points^{3,6}. However, many of these arrays in forms of 3×3, ^{13,18,29} 4×4, ^{8,15} 5×5, 9 6×6, 30 and 8×810 suffer from low resolution and/or crosstalk between neighboring elements resulting in low quality pressure maps. To overcome these issues, high-density arrays³¹ or specially engineered electrode systems, such as integrated coplanar electrodes,²¹ have been implemented. Recently, some true 2D pressure visualization sensors have been established with the incorporation of electrical impedance tomography (EIT). 32-34 EIT is a 2D imaging technique that can reconstruct the electrical conductivity distribution within a conductive domain by using voltage measurements collected exclusively from domain boundary electrodes.³⁵ A thin and pressure sensitive composite can serve as this 2D domain to enable EIT-based pressure mapping that reconstructs the pressure-induced local conductivity changes within this domain. In this way, typical limitations associated with sensing arrays such as the internal wiring systems, complex array structures, and physical contacts between electrodes and applied pressure, can be avoided with EIT-based area sensors. 33,34

In this study, we first demonstrate a large-area, super flexible and conformable, and mechanically robust pressure sensor based on a carbon nanotube-based nonwoven elastomeric composite. Specifically, a commercial silicone rubber was chosen as the flexible matrix and an aramid nonwoven textile fabric was selected as the carrier for the nanotube network and the inplane mechanical reinforcement, making the sensor robust. A straightforward fabrication method consisting of a dip-coating process for coating the fibers followed by infusion of silicone is used to create the flexible sensing skin. The sensor response was examined under a variety of loading conditions to establish the linearity, sensitivity, and dynamic range. Notably, a 2D EIT-based modality for spatial pressure mapping was realized with 12.7×12.7 cm skin sensors. A series of static weight-stacking tests were conducted to validate its performance. The EIT maps demonstrate accurate results for the location, shape and amplitude of the spatial pressure with single contact area, but result in larger errors in mapping the pressure with multiple contacts. Unlike many sensors reported in the literature, the use of commercially available and wellestablished materials combined with conventional coating and composites manufacturing offers the potential for straightforward and efficient process for large-scale production of these flexible pressure sensors.

2. EXPERIMENTAL METHODS

2.1 Materials, Manufacturing and Sensor Preparation

A commercially available nonwoven fabric consisting of randomly distributed discontinuous para-aramid fibers (12 mm fiber length) with a cross-linked polyester binder was selected as the carrier for the electrically conductive network. The nonwoven fabric has an areal weight of 50 g/m² and a thickness of 0.78 mm (Technical Fiber Products, Inc., Schenectady, NY, USA). An

aqueous CNT-containing sizing agent having approximately 1.5 wt% nanotubes, 3 wt% surfactant, and 1.5 wt% film former (SIZICYLTM XC R2G, Nanocyl, Belgium) was used to create a conductive coating on the fibers. A platinum-catalyzed silicone elastomer (Ecoflex® 00-20, a Part A/B kit, Smooth-On, Inc.) was used as the polymer matrix. Conductive silver paint (SPI Flash Dry, Structure Probe, Inc.) and silver-filled conductive adhesive (EPOXIES®40-3900, Epoxies, Etc.) were used to create electrodes on the sensor.

The overall composite sensor manufacturing procedure is outlined in Figure 1. The fabrication of nonwoven sensing fabric with a dip-coating process has been established in our previous work. 36-38 The CNT coating was applied to the fibers by first diluting the as-received sizing with a weight ratio of 1:2 sizing:ultrapure water. To ensure that there is a uniform dispersion of the diluted sizing the mixture was processed using a centrifugal mixer (THINKY® ARM-310) at 2000 rpm for 2 minutes followed by bath sonication (Branson® 1510) for 20 min. The nonwoven aramid fabric was dipped in the CNT dispersion for 20 minutes followed by drying in a convection oven at 160°C for 1 hour. Importantly, prior to impregnation of the silicone matrix, electrodes were applied to the CNT coated fabric using silver paint and wires anchored with silver epoxy to ensure good electrical connections between electrode wires and the sensing fabric.

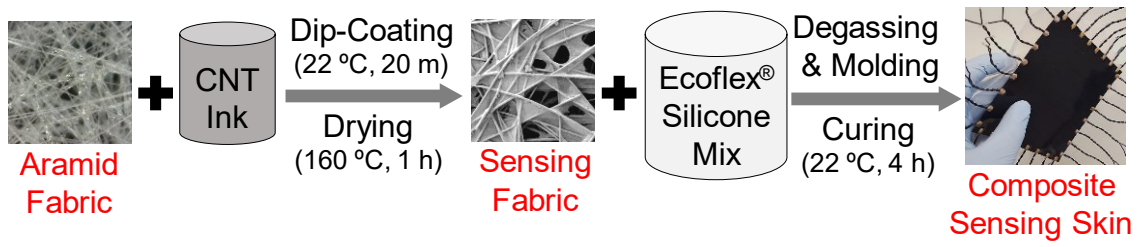
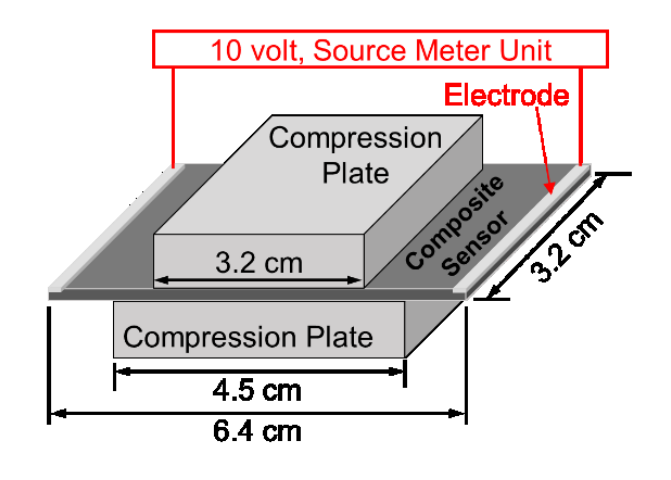


Figure 1. Flowchart showing the key procedures for manufacturing aramid-CNT-silicone composite sensors.

The composite sensors were fabricated by mixing the silicone elastomer (Part A) with the crosslinker (Part B) at 1:1 weight ratio and soaking the CNT-coated fabric in the mixture while degassing for 20 minutes in a vacuum oven to remove air bubbles. Next, the silicone-impregnated samples were molded between two flat aluminum mold plates with 1.2 mm thick spacers to maintain a uniform thickness. A metal weight was placed on the top mold plate to squeeze out excess silicone and ensure all sensors have a uniform thickness of 1.2 mm. Samples were then cured at room temperature for 4 hours and followed by post-curing in a convection oven at 80°C for 2 hours and 100°C for one hour. Based on weight difference calculations before and after manufacturing, the aramid-CNT-silicone composite has a fiber volume content of approximately 9.8 vol.% and a CNT concentration of approximately 0.35 wt%.

As illustrated in Figures 2a and 2b, sensors with two different electrode configurations were fabricated – a 2-electrode distributed pressure sensor $(3.2 \times 6.4 \text{ cm})$ and a 32-electrode skin sensor $(12.7 \times 12.7 \text{ cm})$ for pressure mapping. Two groups of control samples including an aramid-silicone composite and unreinforced silicone films were prepared under the same conditions and size.



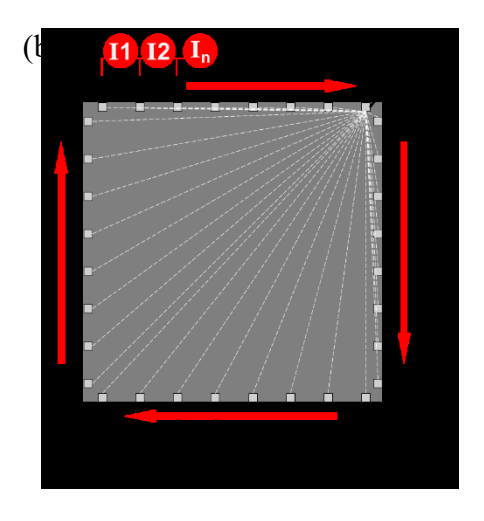


Figure 2. Schematic illustrations showing (a) the setup for electromechanical characterization with point-type sensors using two identical compression plates (resulting in two compression areas of 3.2×3.2 cm and 3.2×4.5 cm), and (b) the hybrid adjacent current-voltage measurement pattern for EIT-based pressure mapping using skin sensors with 32 boundary electrodes (current injection route shown by arrows around the boundary, and voltage measurement pathways as dashed lines within the domain).

2.2 Microstructure Characterization

A handheld digital microscope (Dino-Lite® AM4113ZT, Dunwell Tech, Inc) was utilized to examine the structure and quality of the coating on the aramid fabric prior to resin infusion. The morphology of CNTs, aramid fibers and the fractured aramid-CNT-silicone composites was characterized using an AURIGATM 60 CrossbeamTM FIB scanning electron microscope (SEM) with an acceleration voltage of 3 kV. Composite samples were cryo-fractured in liquid nitrogen and a thin layer of Au/Pt was sputter coated onto the fracture surface (Denton Desk IV, Denton Vacuum LLC) to minimize charging.

2.3 Mechanical and Pressure Sensing Performance Characterization

The sensing response of the composite sensors and the mechanical response of the control samples were examined using a screw-driven universal testing machine (Instron 5567) with a 30 kN load cell. Monotonic normal pressure was applied to the samples by two polished parallel compression plates (shown in Figure 2a with the compression area of 3.2×3.2 cm) at a displacement rate of -0.4 mm/min. To ensure complete failure of all samples, the ultimate

compressive displacement was set to -1.1 mm -- 92% of the sample thickness. Here, all samples could freely dilate laterally under compression. Pressure sensing performance was evaluated by measuring the electrical response in real-time with applied pressure across the composite sensors using a two-probe method (Figure 2a) using a source meter unit (Keithley 6430, Keithley Instruments Inc.) by applying a source voltage of 10 V and measuring the current. Based on Ohm's law, the transient electrical resistance (R) was recorded and the normalized resistance change calculated by the percentage bulk resistance change of the sensor: $\Delta R/R_{\theta}$ (%) ($\Delta R = R-R_{\theta}$ and R_{θ} is the initial electrical resistance).

Being consistent with other studies, ^{1,2,6} the pressure sensitivity of the sensors was defined as the normalized resistance change due to the unit pressure change and calculated as $[\Delta R/R_0]/\Delta P$ (ΔP is the transient pressure change) that can be represented by the slope of the resistance change versus pressure curve. In the the compression tests R_0 was measured prior to application of load. For nine sensors the average R_0 and measurement standard deviation was $337 \pm 28 \Omega$. The initial volume electrical resistivity, ρ_0 , and conductivity, σ_0 , of the composite sensors were then calculated to be $0.225 \pm 0.019 \Omega$ -m and $4.44 \pm 0.38 \text{ S/m}$, respectively by $\rho_0 = R_0 \times A/L$ and $\sigma_0 = 1/\rho_0$ (A is the cross-section area of the sensor and L is the gage length between the two electrodes).

After confirming the elastic working range of the composite sensors from the monotonic testing results, a series of cyclic compression tests were conducted to evaluate the sensor performance under differing pressure ranges. Samples were first subjected to an incremental quasi-static loading-unloading protocol with the compression area of 3.2 × 4.5 cm at a constant displacement rate of -0.5 mm/min and with load peaks of -200, -300, -450 and -600 N that exerts -136, -204, -306 and -408 kPa pressure, respectively. Each load peak was repeated four times

with a six-second hold between each threshold. Next, a 0.1-Hz cyclic loading test was performed using a servo-electric universal testing machine (Instron 8562) with a 15 kN load cell. Samples were compressively cycled 30 times within both low and high pressure ranges including -100 to -600 N (-95 to -570 kPa) and -1 to -2.5 kN (-0.95 to -2.4 MPa) cycle with the compression area of $3.2 \times 3.2 \text{ cm}$ at a loading rate of -100 N/s (-94.7 kPa/s) and -300 N/s (-284.1 kPa/s), respectively. At least five samples were tested for each loading scenario to ensure measurement accuracy and repeatability.

2.4 Tomographic Approach and Testing for Spatial Pressure Mapping

After characterizing the basic pressure sensing properties, the spatial pressure mapping capability of the aramid-CNT-silicone composite sensors were studied with the EIT framework as established in our previous work. 38,39 To obtain EIT maps of conductivity distributions, both forward and inverse problems need solved sequentially. The forward problem is the process of numerically simulating the boundary voltages with a preselected initial conductivity and normally executed using the finite element (FE) method. 35,40,41 The mathematical model is governed by Equation (1) with boundary conditions enforced by the complete electrode model (CEM). 40,42,43

$$\nabla \cdot (\sigma \nabla u) = 0 \text{ (in 2D domain)} \tag{1}$$

where, σ is the conductivity distribution and u is the voltage.

The weak solution to Equation (1) is estimated by the discrete FE model that is generally expressed by a linear system of equations as following:

$$\begin{bmatrix} A_M + A_Z & A_W \\ A_W^T & A_D \end{bmatrix} \begin{bmatrix} u \\ U \end{bmatrix} = \begin{bmatrix} 0 \\ I \end{bmatrix}$$
 (2)

where $[A_M]$ is the usual system matrix for Equation (1); $[A_w]$, $[A_D]$ and $[A_z]$ set CEM boundary conditions.^{35,46}

With the computed nodal voltage distribution [u], the Jacobian matrix [J] can be constructed to relate changes in boundary voltages at electrodes to internal conductivity. Next, the inverse problem reconstructs the internal conductivity distribution with the known set of injected currents [I] and boundary voltage measurements [U]. It is known that this is an ill-posed and nonlinear inverse problem. To impose the regularization and linearity, a one-step difference imaging algorithm, namely the maximum a posterior (MAP) given in Equation (3), 44 was employed to reconstruct the map of normalized conductivity changes $([\Delta \sigma/\sigma_0])$.

$$\left\{\frac{\Delta\sigma}{\sigma_0}\right\} = \left[(J^T W J + \lambda R)^{-1} J^T W \right] \left\{\frac{\Delta U}{U_0}\right\} = B \left\{\frac{\Delta U}{U_0}\right\}$$
 (3)

where, $[J]_{ij} = -\int \sum_{i=1}^{2} (\nabla u)_i (\nabla u^*)_j dxdy$, $^{40}[W]$ is the covariance matrix for voltage measurements; [R] is the regularization matrix; λ is the regularization parameter; [B] is the reconstruction matrix corresponding to a specific λ ; $[\Delta U/U_0]$ presents the normalized change of voltage measurements with $\Delta U = [U] - [U_0]$.

Specifically, Tikhonov regularization^{35,40} was used to treat the ill-posedness of the inverse problem by imposing smoothness. The extent of smoothing is controlled by the selected λ . Here, the finally stabilized reconstruction without under- or over-smoothness is computed with the optimal λ (λ_{opt}), which is determined when implemented noise figure (*NF*) equals to 1.⁴⁵ It is worthy to note that the *NF* metric, first introduced by Adler *et al.*⁴⁴ sets the signal-to-noise ratio of the reconstructed conductivity distribution (*SNR*_o) be proportional to the *SNR* of the voltage

measurements (SNR_U) (i.e., $NF = SNR_U/SNR_\sigma$). Additional details related to the EIT method are reported in our previous research.^{38,39}

Skin sensors (12.7 \times 12.7 cm) were fabricated with 32 electrodes anchored around the boundary as shown in Figure 2b. The initial conductivity of these samples were measured in their horizontal and vertical directions. Spatial pressure were applied on the sensor by statically stacking metal weights at different locations. Different pressure regimes (< 32 kPa) were deployed accordingly to demonstrate the capability of EIT-based pressure mapping. Here, EIT measurements were taken following a hybrid adjacent current-voltage scheme³⁸ as shown in Figure 2b where 32 current injection pairs (starting with I1 between electrodes #1-#2) are sequentially applied around the boundary and the resulting differential voltages (dashed lines) are measured in reference to the preselected ground electrode #8. Note that for all current injections (I1 to I32), the collection of voltage measurements remains in the single-ended pattern. Before and after a pressure event, a full EIT data set of 870 (29×30 without involving the ground and current injection electrodes) independent voltage measurements were collected using a customized data acquisition system consisting of a sourcemeter (Keithley 6430), multiplexer (Keithley 3706A) and nano-voltmeter (Keithley 2182A)^{38,39} with 10 mA direct current injections applied. Utilizing the previously established 2335-element FE platform in a MATLAB environment⁴¹, EIT reconstruction maps were computed after each event to display the pressureinduced conductivity changes occurred in the skin sensor.

3. RESULTS AND DISCUSSION

3.1 Composite Structure and Morphology

The materials selected for the pressure sensor were chosen to allow through-thickness deformability by utilizing a silicone elastomer while having in-plane dimensional stability because of the high modulus aramid fibers. The in-plane stiffness prevents excessive resistance changes due to extensional deformation, ensuring that the sensor response is dominated by outof-plane pressure. The hybrid composite sensor demonstrates excellent flexibility and conformability. Figure 3a shows an 8 × 102 mm sensor rolled around a 6 mm diameter tube, and in Figure 3b the same sensor is folded seven times, reaching a bend radius down to 0.5 mm. This deformed strip easily reverts back to its original shape without any damage (Figure 3c). This formability of the composite sensing skin offers opportunity to conform the sensor to complex shaped surfaces. It should be noted that the sensor's electrical response due to large bending and folding motions has been preliminarily studied and demonstrated a stable trend of resistance change after 60 bending- and folding-releasing cycles (see Figure S1 in supporting information), showing the comparable variations as those recently reported textile sensors.⁴⁷ In this research we examine the sensing response of a planar sensor. If the sensor is conformed around a surface there will be a resistance change due to the in-plane deformation (Figure S1) that would need to be compensated for.

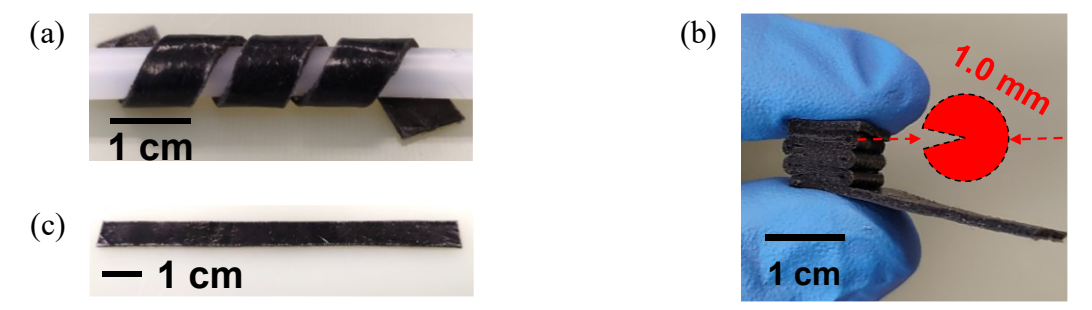
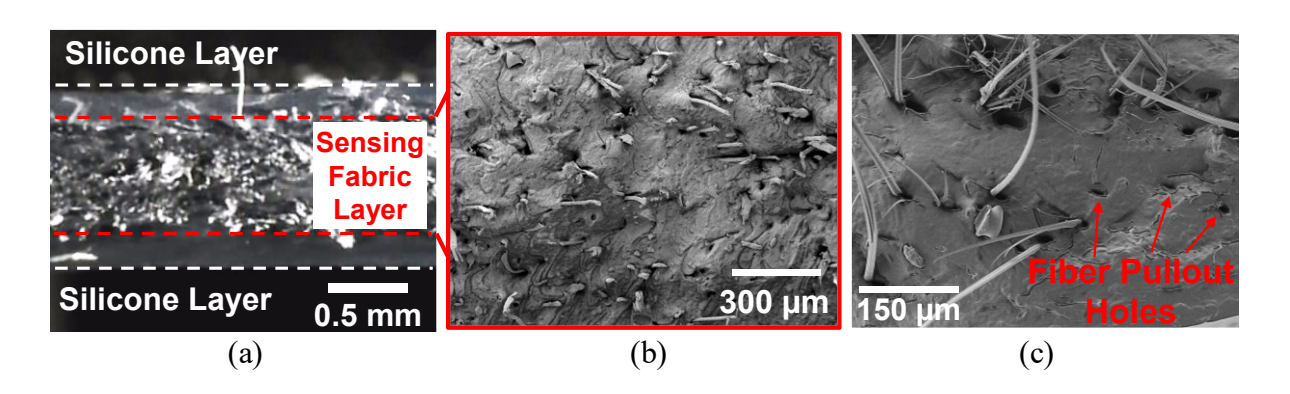


Figure 3. Photographs showing an 8×102 mm composite sample (a) twisted on a 6 mm-dia. tube, (b) folded 7 times and pressed between fingers, (c) recovered after a,b.

Figure 4a shows a cross-sectional optical micrograph of the composite sensor, which shows the fabric sensing layer (~ 0.8 mm) at the center of the composite and thin (~ 0.2 mm) silicone rich layers at the surfaces. The silicone fully encapsulates the textile sensing layer, creating a protective barrier against moisture and other chemicals and creates an electrically insulating, safe substrate for skin contact applications. Figure 4b shows an SEM micrograph of the freezefractured surface of the silicone-infused sensing layer, revealing a composite structure of randomly distributed fibers with a low overall volume fraction. Figure 4c shows a typical area on the fracture surface where some splitting fibers are protruding from the matrix and have relatively smooth fiber surfaces due to the stripping of CNT coating layer which remains in the pullout holes. This suggests that during fracture the debonding likely occurs at the interface between the CNT coating and the fiber surface. In addition, Figure 4d shows a micrograph of the fractured composite sensor where the silicone-rich layer had peeled-away. It can be seen that the interconnected fibrous network is infused with silicone and on the fracture surface imprints of peeled-off fibers can be seen in the silicone rich region. Some irregular pores (~50-350 μm) appear near the fiber-fiber connecting regions, resulting in a macro porous hierarchical structure that may enhance compressibility. 11,18,19 Figure 4e shows a high magnification image of a coated fiber that has debonded from the matrix and embedded CNTs on the fiber coating are clearly visible with little or no CNT pullout.



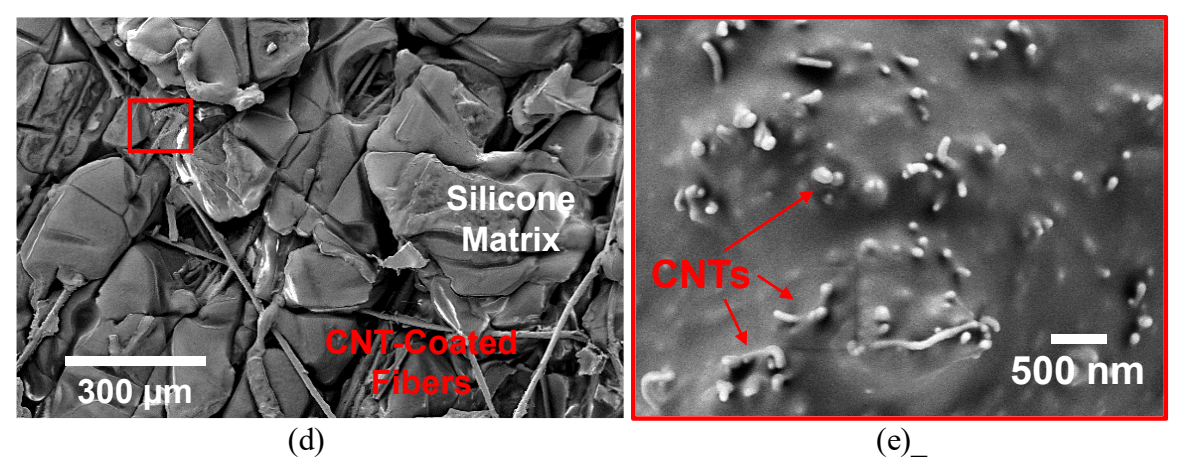


Figure 4. (a) An optical image showing the cross-section of the composite sensor and SEM micrographs showing (b) the sensing core region, (c) the splitting fibers and fiber pullout holes, (d) in-plane view of the hierarchical composite structure, and (e) the enlarged view of the boxed region in (d) showing the morphology of nanotube coating on fiber surfaces.

3.2 Mechanical Properties

Figure 5a shows the through-thickness mechanical response of the pure silicone, aramid-silicone, and aramid-CNT-silicone (the sensor) as statically compressed. It can be seen that pure silicone film shows the lowest strength but a highly elastic behavior with a strong linearity observed before approaching 0.4 mm (33.3% compressive deflection at a pressure 850 kPa). As pressure further increases, the compressive response deviates from the original linearity due to the yielding of the unreinforced silicone film, demonstrating unrestrained dilation out of the compression plates, as shown in the inset of Figure 5a. Both composite films show a similar response consisting of three distinct regions including a linear elastic region, the highly nonlinear region with possible silicone matrix yielding and fiber-matrix debonding, and a final linear region of fabric crushing, shown by the limits A and B labeled in Figure 5a. In the region between A and B on the pressure-displacement graph, there are localized load drops, which may

be indicative of a stick-slip debonding mechanism between the fibers and the silicone matrix. It should be noted that due to the reinforcement from fibers and nanotubes, the as-prepared sensor show the average elastic compressive deflection of 25% (i.e., 0.3 mm) at 5.8 MPa and final compressive strength of 11.2 MPa, which is over 200% and 35% greater than these limits of the aramid-silicone films and 650% and 350% higher than the unreinforced silicone films.

The corresponding deformed shape of composite samples are represented in Figures 5b-d. As compared to the pure silicone, the out-of-plane dilation is constrained by the in-plane aramid fiber network, resulting in enhanced compressive behavior. At the elastic limit A, both composite films display a uniform bulging shape with small bubbles formed along the edge (Figure 5b), possibly resulting from the relocation of the embedded air pores under compression. 10 With increasing compression, the silicone matrix likely debonds from fibers and initiates permanent damage, limiting load transfer and causing the decreasing the bulk stiffness. Clearly, at the yielding limit B, a large amount of material is squeezed out of the compressed plane (Figure 5c), showing a distorted, bulging shape. At higher displacements the aramid fiber network undergoes transverse deformation until final compression failure, as shown in Figure 5d. Schematics describing the deformed shapes are shown in Table S2 in supporting information. In short, the high elastic limit compared to the silicone and aramid-silicone demonstrates the robustness of the pressure sensor. Additionally, in our previous work³⁷ under the in-plane tension loads, this aramid-CNT network in an epoxy matrix has also displayed stable mechanical properties as commonly observed in nanoengineered fiber composites.⁴⁸

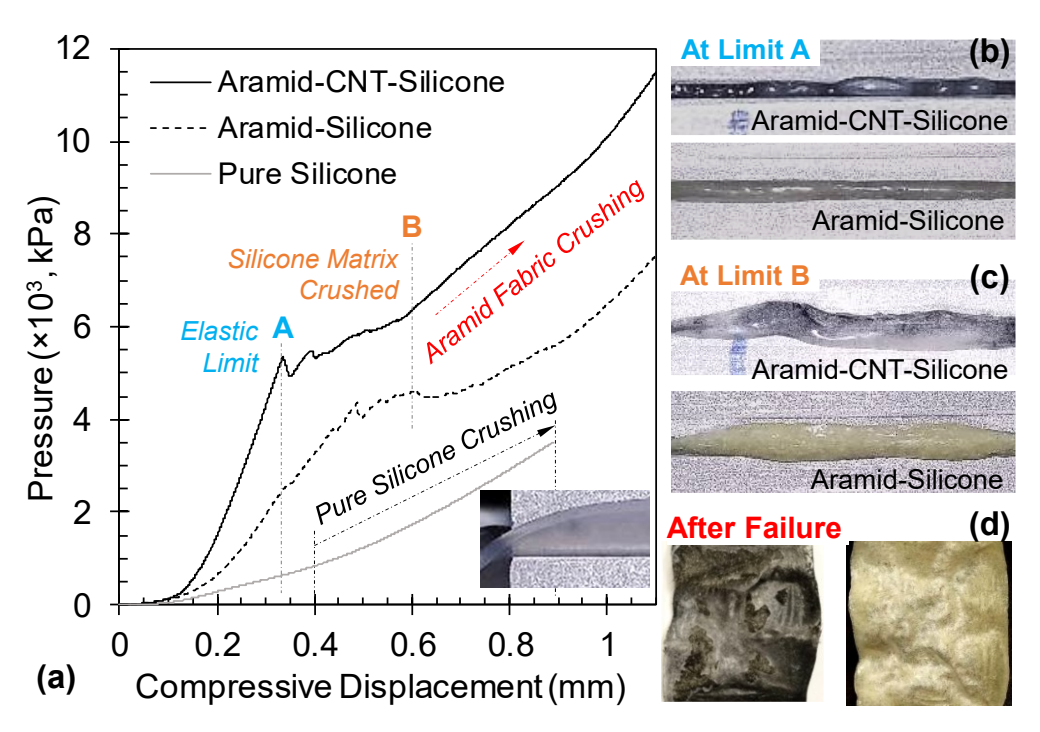


Figure 5. (a) Typical compressive mechanical responses of aramid-CNT-silicone (the sensor) and aramid-silicon composites, and pure silicone (with its crushed shape shown in inset), and (b,c,d) corresponding snapshots showing the deformed shapes of the composite samples at A, B, and the final failure stage.

3.3 Electromechanical Response for Pressure Sensing

Figure 6a shows the typical real-time resistive response of the pressure sensor under monotonic compression. As expected, the sensor response (solid, red line) closely follows its mechanical behavior (black, dashed line), demonstrating the three characteristic regions as previously mentioned (Figure 5). As the applied pressure increases, the resistance change of the sensor increases instantly, showing a monotonous positive pressure correlation (PPC). In our sensor, the CNT network is continuously coated on a nonwoven fabric and develops a certain amount of junctions between fibers. As shown in the micrographs in Figure 4, the CNT coating and the associated fiber junctions are surrounded by the insulating silicone matrix. The resistance change

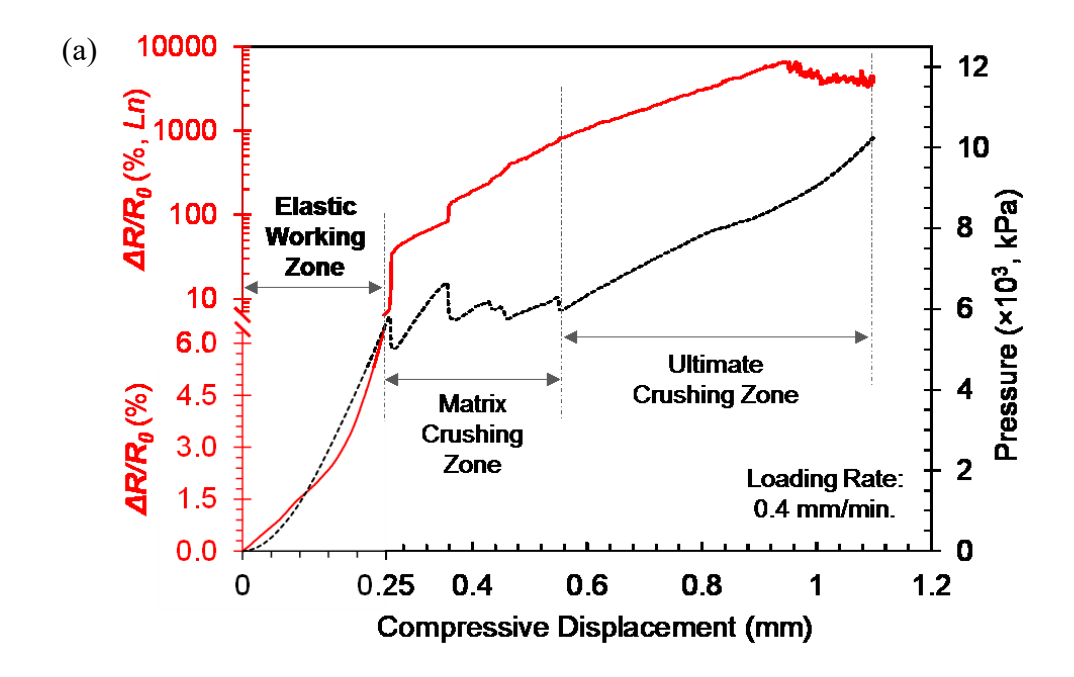
mechanism is likely the in-plane straining of the piezoresistive CNT network on the fiber surface due to Poisson expansion/dilation under out-of-plane pressure. This is a similar mechanism as observed by Wu et al.²⁹ for a sandwich sensor of vertically aligned graphene nanosheets and PDMS where they show a very good agreement for predicted values based on Poisson expansion under out-of-plane compression with their experimental results. Meanwhile the silicone likely insulates the individual fibers from making any conductive junctions, resulting in PPC behavior. For comparison, similar sensors investigated by Doshi and Thostenson²⁶ where a nonwoven aramid fabric with an electrophoretically deposited CNT coating without a supporting matrix of silicone displayed a decrease in the in-plane resistance under pressure, or a negative pressure correlation (NPC). This resistance change was attributed to the junction-dominated conduction mechanism from (1) the distributed fiber-fiber junctions at low pressure and (2) the fiber-fiber piezoresistive response of the sponge-like porous nanocomposite coating under compression. It should be noted that a group of six samples demonstrated the similar PPC behavior with a remarkable elastic working limit of 5.5 ± 0.5 MPa. Above the elastic limit, we observe an initial load drop and instantly observe large jumps in the resistance that directly correspond to load drops. We believe that this is likely due to matrix yielding and fiber/matrix debonding accompanied by severing of in-plane conductive pathways on the fiber surface. At higher pressures, there is continued increase in resistance and appears to reach a maximum prior to the applied deformation limit, resulting in an overall 6700% resistance change.

Figure 6b shows the electromechanical response where the resistance change of the sensor is shown with applied pressure. The overall sensing response (solid, red line) with pressure is nonlinear but responsive up to its elastic limit, enabling a large dynamic range of the sensor. This response can be fitted to a cubic curve (gray, dashed line) with a correlation coefficient of 0.999

(Figure 6b). Clearly, the sensor shows pressure-dependent sensitivity, which is in agreement with most of the reported studies. ^{17,21,49} In addition, this working range can be segmentally linearized in multiple pressure regions covering the 0.2-1.1 MPa, 1.1-3.3 MPa, and 3.3-5.5 MPa with the linearized sensitivity of 0.01, 0.0068, and 0.015 MPa⁻¹, respectively. Notably, the high sensitivity is demonstrated at low pressures (highlighted in yellow in Figure 6b). For instance, as enlarged in Figure 6c, the sensor displays a sensitivity of 5×10⁻⁵ kPa⁻¹ (0.05 MPa⁻¹) in 2-50 kPa range and 1.7×10⁻⁴ kPa⁻¹ (0.17 MPa⁻¹) in the tactile range below 2 kPa as shown in the inset of Figure 6c. Although the elastic pressure sensitivity of this sensor is lower than other CNT-based flexible sensors highlighted in the introduction and those recently reported by Yang *et al.*⁶ and Li *et al.*⁵, the working range of the current sensor is 2-3 orders of magnitude larger and is highly scalable for large-area sensing applications.

To establish a viable pressure sensor, it is necessary to evaluate the sensor performance under multiple cycles. Figure 7a shows the real-time sensor response as subjected to the incremental pressure cycles. Within the applied 0-400 kPa pressure range, the resistive response (red line) displays a stable and elastic trend with local minima and maxima consistent to the individual peak and valley loading points (dashed line), displaying a strong correlation with the pressure profile. In addition, a resistance change (~0.4%) is observed after the first cycle, which is likely due to the irreversible self-adjustment of the composite structure when initially compressed and also corresponds slight permanent residual displacement (gray line). This phenomenon vanishes in subsequent cycles and reappears as the sensor subjected to an increased pressure level, is similar to that observed in references^{49,50} along with commercial point-type sensors,⁵¹ which must be pre-loaded up to the maximum desired sensing range and then are repeatable after that. Figure 7b shows the electromechanical response corresponding to the 2nd ramp of the 200, 300

and 400-kPa pressure cycle, which exhibits a linear elastic trend with the nearly identical pressure sensitivity quantified as 0.031, 0.029 and 0.028 MPa⁻¹, respectively. Upon complete unloading, there is a slight resistance drift observed in the pressure-holding period likely due to the viscoelastic relaxation of the silicone matrix.^{30,52,53} Note that about 20% variation in pressure sensitivity was shown by the tested samples, which likely results from the intra/inter-batch variations of the samples.



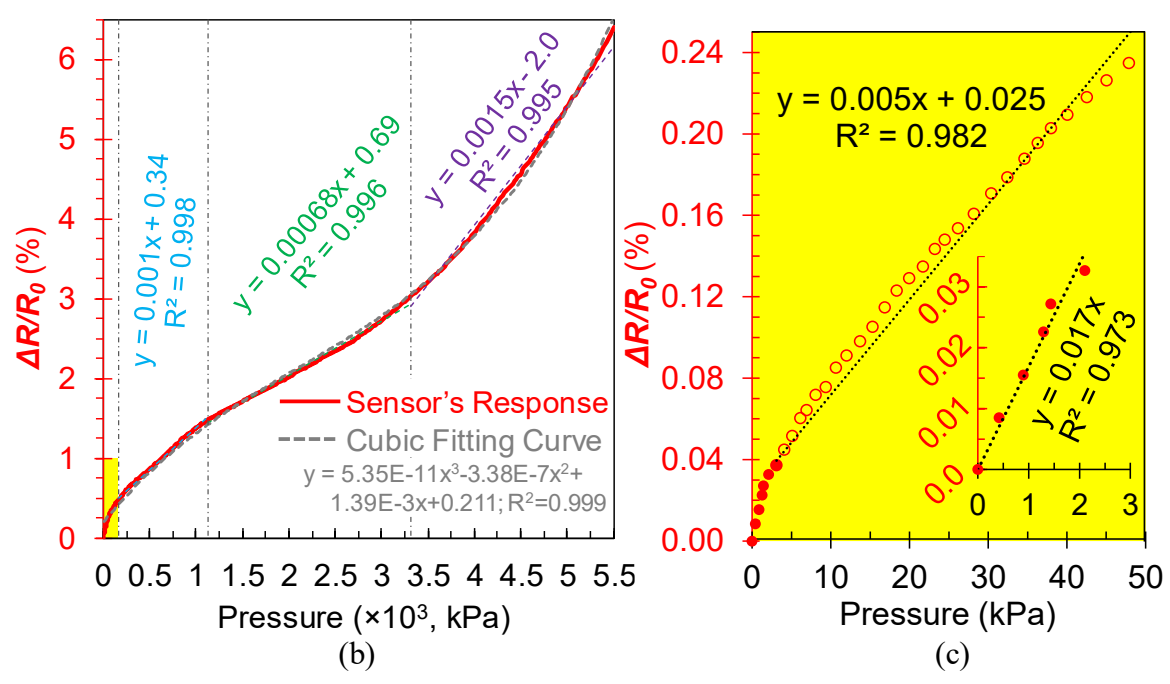


Figure 6. (a) Typical real-time resistive response (solid red) of the sensor as compressively loaded to 92% deflection (1.1 mm) in comparison with its mechanical behavior (dashed), showing an elastic working range up to 5.5 MPa the vertical axis switches from linear to logarithmic after the elastic, (b) the corresponding sensors' electromechanical response within its elastic working range with linearized curves indicating the pressure sensitivity in consecutive pressure ranges, and (c) enlarged view of the low pressure response (< 50 kPa) in (b) (yellow shadowed zone) with the close-up view of tactile pressure range (< 2 kPa) shown inset.

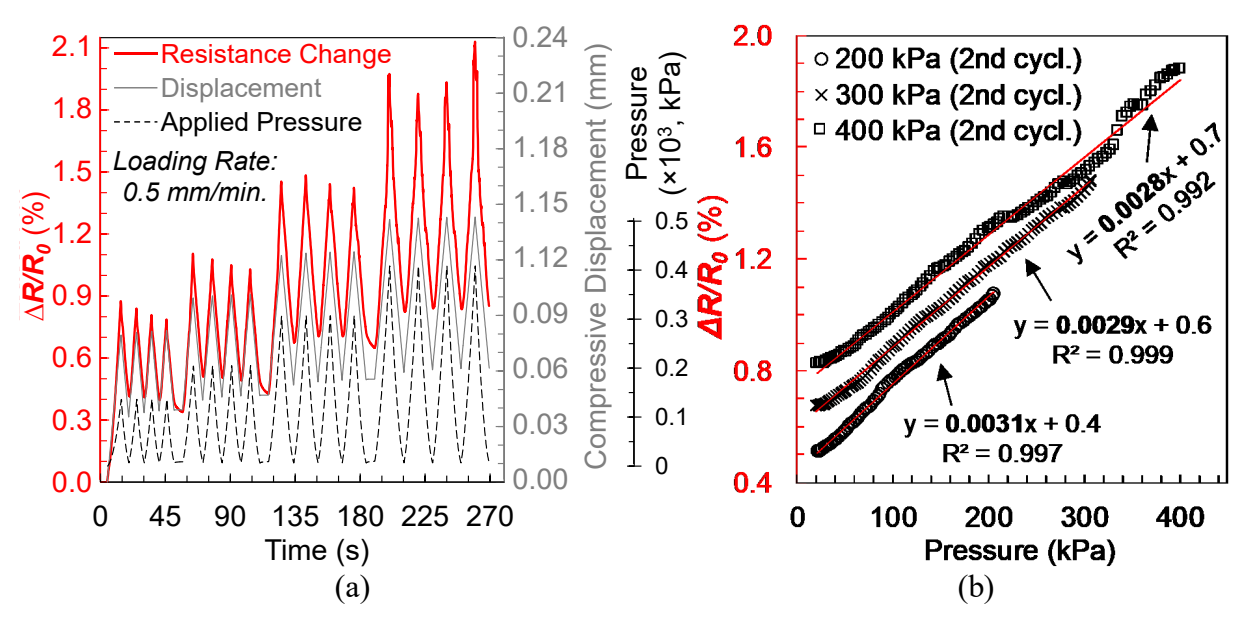


Figure 7. (a) Typical real-time resistive response (solid red) of the composite sensor under a displacement-controlled incremental cyclic pressure protocol (black dashed) in comparison with its mechanical behavior (solid gray) and (b) the sensors' electromechanical response corresponding to 200, 300, and 400 kPa pressure cycles with linear curve fits indicating the pressure sensitivity.

The pressure sensor performance was further explored under the load-controlled repeated pressure cycles. Figure 8 shows the typical resistive response in the 100-600 kPa and 1.0-2.4 MPa pressure range for 30 repeated cycles at 0.1 Hz. Consistent with the previous tests (Figure 7a), the initial drastic resistance change is observed during the first cycle in both pressure ranges. Later, the sensor shows a close correlation with the applied pressure cycles but also an overall time-dependent drift, likely due to the viscoelasticity of the silicone matrix. Similar dependence is commonly observed in the responses of the CNT-based flexible sensors. ^{49,54} After 20 cycles, the resistive response tends to stabilize and demonstrates a nearly constant resistance change of 0.13% and 0.25% in the 100-600 kPa and 1.0-2.4 MPa pressure range respectively, indicating the repeatability of the sensor. We also believe that this tendency may be dominated by the structure

modulation process of the sensor,⁵⁵ which means that over a few loading-unloading cycles the fiber skeleton fully interacts with the applied pressure after the relocation of embedded pores (Figure 4d), creating a steady conductive network. This process is related to the fatigue behavior of the sensor and will be explored in future research.

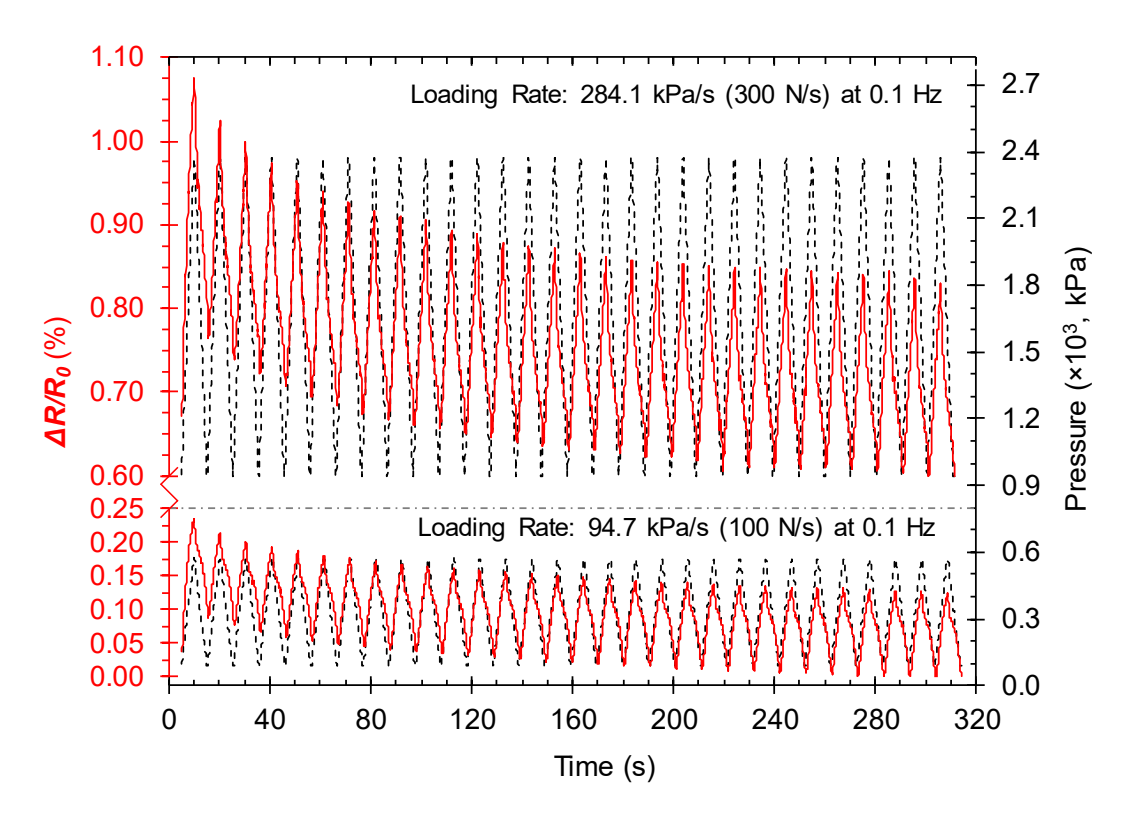


Figure 8. Typical real-time cyclic response (red) of the composite sensor in 1.0-2.4 MPa (top) and 100-600 kPa (bottom) pressure range under load-controlled pressure protocols (dashed).

3.4 Spatial Pressure Mapping

For many practical pressure sensing/monitoring applications, it is desirable to visualize the spatial pressure distribution as readable graphics. Because the electrical properties of the composite pressure sensor are globally in-plane isotropic, we can utilize the EIT technique for a

true 2-D pressure sensing modality to relate local electrical property change to the applied pressure. To evaluate the feasibility and performance of the sensor to map pressure distribution, the sensors were evaluated under multiple test conditions with defined pressure amplitudes and contact areas. Because the composite sensor demonstrates measurable sensitivity in the low-pressure range (see Figure 6c), the applied local pressure amplitudes were limited to 32 kPa to evaluate the ability of the larger sensing skin to detect low pressures. This pressure range is also common for human daily activities,² such as gentle manipulation of objects and walking. Selection of the pressure contact area size was based on the nominal spatial resolution of the EIT method $(3.4\% = 1/\sqrt{N}=1/\sqrt{870})$, where N is the number of independent measurements).³³ For all tests the initial conductivities of the square sensing skins were measured prior to application of pressure so that the calculated electrical conductivity map could be normalized relative to the initial conductivity.

In order to validate the ability of the sensor to detect local pressure amplitude, weights were stacked on the same circular pressure contact area of 1295 mm² located at the center of the specimen. The mass of the weights correspond to pressure amplitudes of 7.6, 14.0, 17.8, 21.6 and 28.3 kPa. The compressed area ratio (CAR) is 8% (pressure contact area/total sensing area = 1295 mm² / (127 mm ×127 mm)) is greater than the calculated nominal EIT spatial resolution of 3.4%. Figures 9a-e show photos of the sensor with different weights stacked on a circular area with increasing pressure amplitude and the corresponding normalized conductivity EIT maps. The contact area is shown by a dashed circle in the EIT reconstructions.

In all of the EIT maps the local electrical conductivity decreases at the location of applied pressure, represented by the color intensity from red to blue, which corresponds to an increase in the local electrical resistance due to the applied pressure observed in the tests on sensors

subjected to uniform applied pressure (Figure 6a). Except for a slight underestimation at the application of 7.6 kPa (Figure 9a), the EIT reconstructions yield accurate results for the pressure location, shape, and amplitude (Figures 9b-e). Note that all EIT maps show sharp contrast, high resolution, and low background noise, which is related to selection of the noise model (i.e., [W] in Equation (3) for white noise³⁸) and λ_{opt} of 0.108 (a relatively high degree of smoothing). The bar charts shown in Figure 9f show the distributions of the total 2335 EIT elements for the color bins ranging from 0 to -0.5% for the five applied pressures. The red bins in the graphs (2300, 2149, 2028, 2063, and 2036 elements) represent the pressure-free zone in the sensing layer, near 0% conductivity change. For the higher pressures the EIT model utilized the rest of the elements (1.5, 8.0, 13.1, 11.6, 12.8% of the total elements) to reconstruct the pressure-induced local conductivity change and estimate the compressed area shown in the EIT maps. For each event, the count of the bin of the largest conductivity change determines the amplitude from -0.1% (orange) to -0.5% (dark blue) for the 7.6 to 28.3 kPa compressions shown in EIT maps.

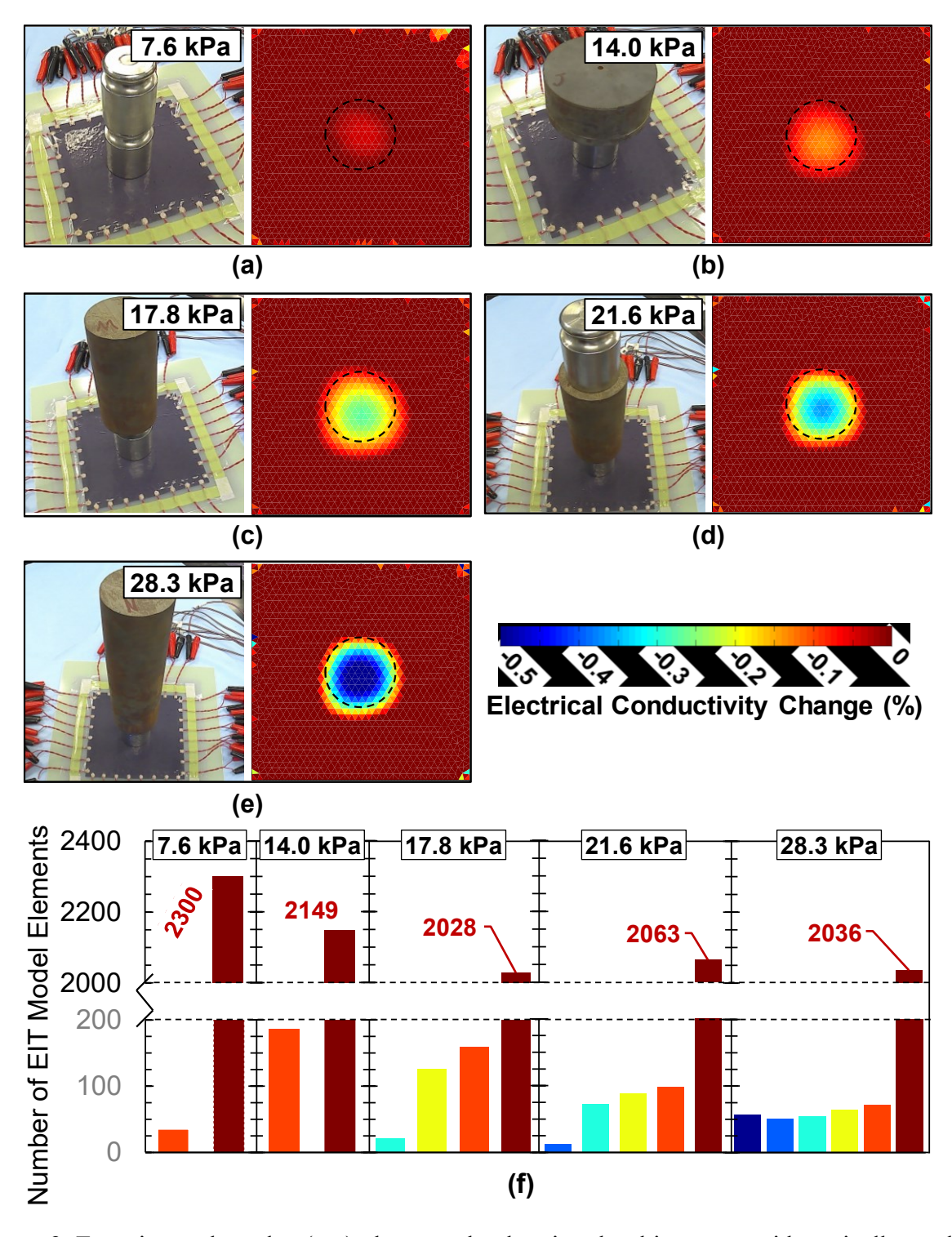


Figure 9. Experimental results: (a-e) photographs showing the skin sensor with statically stacked circular weights at its center with increasing pressure amplitude (7.6 - 28.3 kPa) and the corresponding EIT maps with dashed circulars indicating the actual pressure contact area on the

sensor; (f) bar charts showing the distribution of the total 2335 elements from EIT reconstructions of the five applied pressures.

To examine a uniformly distributed pressure over a large contact area, a large square plate (96 × 96 mm) was placed over the sensor corresponding to 57% CAR. This test evaluates the performance of the EIT method due to the minimal contrastive measurements as a low pressure of 0.87 kPa applied on the sensor (Figure 10a). The EIT map shown in Figure 10b demonstrates relatively low but certainly distinguishable change in color intensity contour under the square area. Some artifacts are observed at the four corners, likely due to the local electrode errors.³⁸ The EIT map is able to estimate the location and shape of contact area, indicating an effectiveness for pressure mapping in the low pressure regime.

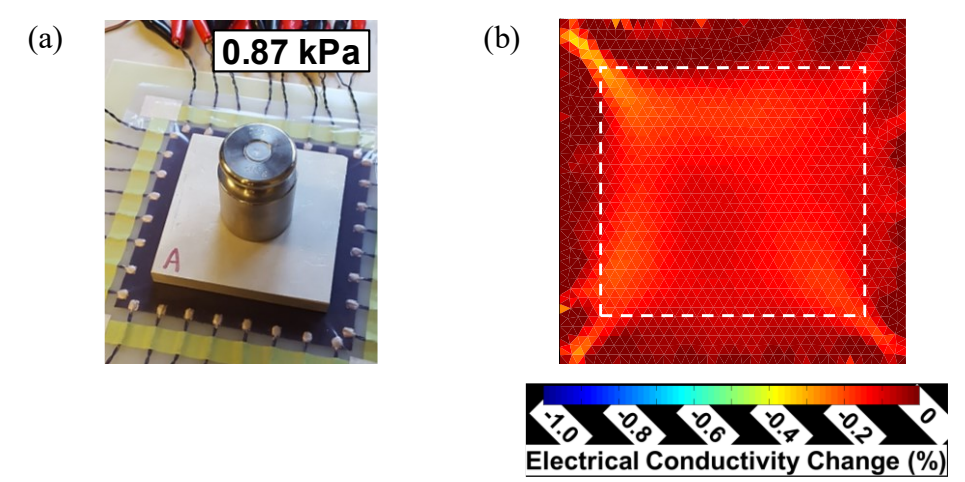


Figure 10. Experimental results: (a) photograph showing the sensor with a square plate and weight added to correspond to a low pressure of 0.87 kPa; (b) EIT map corresponding the applied pressure where the dashed box indicates the actual contact area.

The capability of mapping multiple and distributed pressure locations is also an important performance metric of the sensor. The photographs in Figure 11 show different weights applied where Figure 11a has a single circular contact area with 31.1 kPa pressure that is offset from the

center of the sensor and Figure 11c shows an additional contact area where 26.3 kPa pressure was applied. The two contact areas represent 794 and 1134 mm² of circular contact area for the two scenarios (4.9 and 7% CAR). The corresponding EIT maps (Figures 11b and 11d) show accurate estimations for the pressure locations. It is worthy to note that the second EIT map (Figure 11d) shows an extended transition between the contact areas (dark blue regions) and the color intensity for the 1st applied 31.1 kPa compression is slightly less than the 2nd 26.3 kPa one, which is likely attributed to the temporal error³³ accumulated during these two compression events and also local compressive deformation of the sensor in the region between the two weights due to the low Young's modulus of the silicone. In addition, the EIT model assumes that the sensor has isotropic electrical properties, but the local electrical properties of the sensor are anisotropic due to the random fiber network. The conducting fibers likely intersect the multiple areas of pressure.

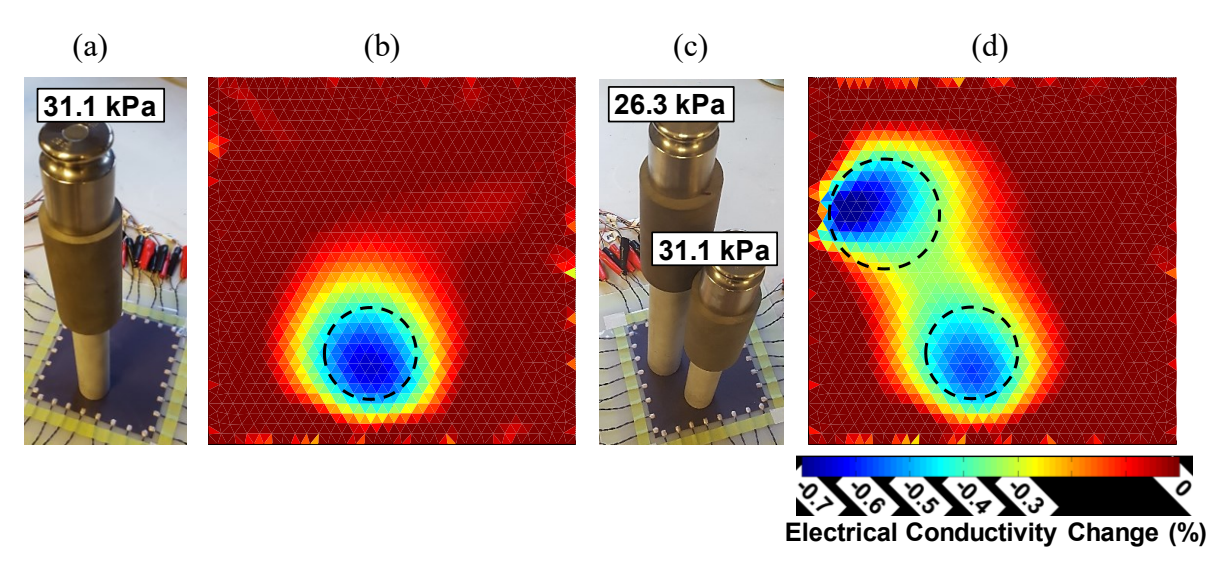


Figure 11. Photographs (a and c) of the pressure sensor with locally applied pressure showing circular contact areas corresponding to 31.1 kPa pressure in a and 31.1 and 26.3 kPa pressure in c, and EIT maps (b and d) corresponding to a, c with dashed circles indicating the actual contact areas.

In another test, three compressions of 10.3, 10.1 and 11.8 kPa with circular contact areas of 1134, 794 and 1552 mm² (7, 4.9 and 9.6% CAR, respectively) were simultaneously applied to the sensor (Figure 12a). Figure 12b shows the corresponding EIT map executed with the Gaussian noise model³⁸ and a much smaller λ_{opt} of 1.18×10^{-6} and shows good qualitative mapping of the pressure locations. With the diminished temporal effect, the three pressure contacts can be visually distinguished. However, the shape of the 10.3 and 11.8 kPa compressions are slightly stretched to the boundary most likely due to electrode contact resistance noise since the pressure contact areas are very close to the boundary electrodes. In addition, the image amplitude for the 10.1 kPa compression is low, likely resulting from the measurement errors caused by shadowing effect that the voltage measurement pathways for the 11.8 and 10.1 kPa events overlapping in the diagonal region (see Figure 2b).

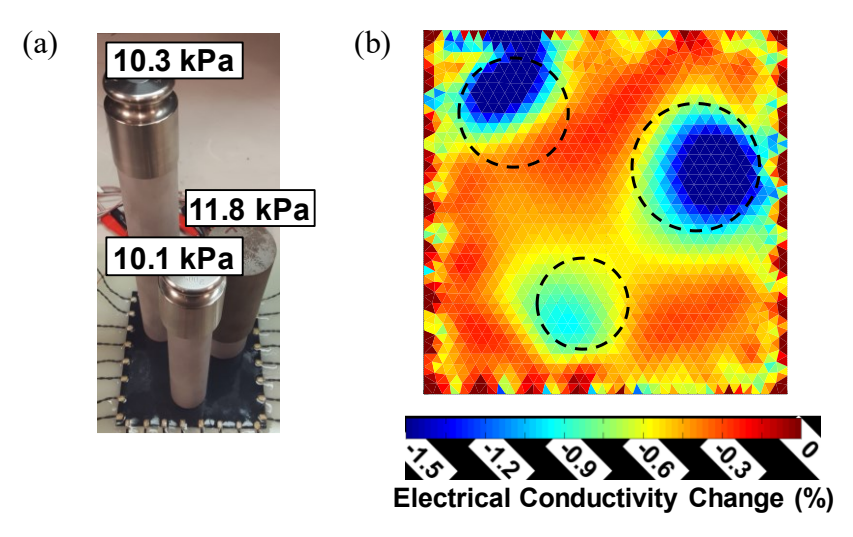


Figure 12. Photograph (a) showing sensor with concurrently applied compressions of 10.3, 11.8, and 10.1 kPa; and (b) the corresponding EIT map with dashed circles indicating the actual contact areas.

To further examine distributed pressure (Figure 13) two specially shaped aluminum weights were used with rectangular contact areas (25×64 mm each, 9.9% CAR) with an uneven pressure

gradient, varying from 8.1 to 2.0 kPa and 7.0 to 0.9 kPa for the 1st and 2nd compression regions, respectively. The EIT maps corresponding to a Gaussian noise model and λ_{opt} of 3.44×10^{-7} are shown in Figures 13b and 13d. With some scattered boundary noise, the reconstructions show reasonable approximations for the location and the rectangular shape of the contact area. Although the area is not a sharp rectangle the bulk electrical conductivity change (yellow to blue) is directly underneath the applied weights with similar shadowing observed with the multiple weight applications. A rough estimate for the pressure amplitude that the color intensities represented for the high end pressure of 8.1 and 7.0 kPa are similar, matching the 1st and 2nd weight contour.

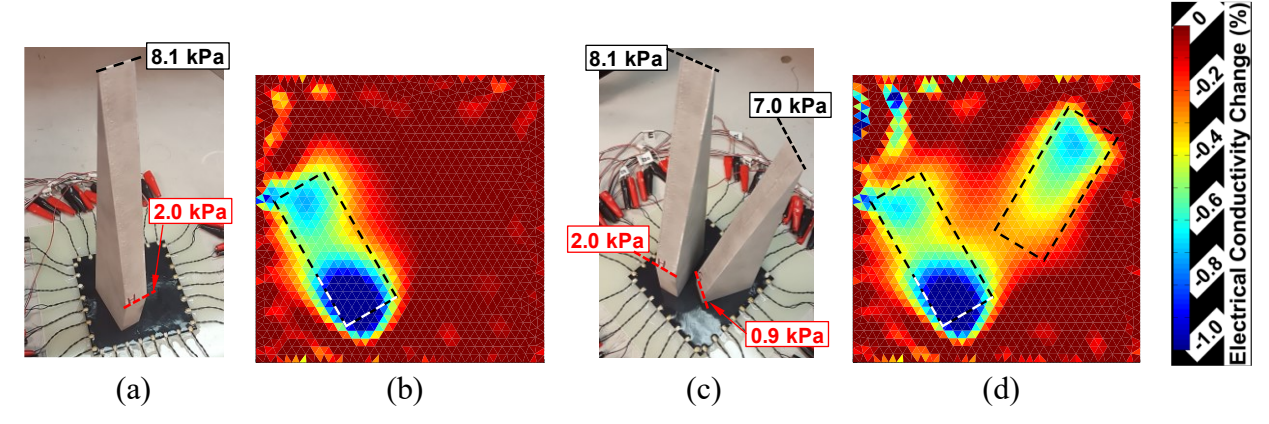


Figure 13. Photographs (a and c) showing with trapezoidal-shaped aluminum weights, inducing one and two rectangular pressure contact areas with varying pressure amplitudes from the high to low end, i.e., 8.1-2.0 kPa in a and 8.1-2.0 and 7.0-0.9 kPa in c; (b and d) EIT maps corresponding to a and c with dashed boxes indicating the exact pressure contact areas on sensor.

4 CONCLUSIONS

In conclusion, we have developed a novel ultra-flexible and conformable composite pressure sensor based on a nonwoven textile carrier coated with CNTs embedded in a silicone elastomer matrix. The sensor is fabricated with straightforward coating and composites manufacturing techniques making it scalable for a wide range of future applications including soft robotics, wearable electronics, human-machine interfaces, biomedical devices, and human motion analysis. The materials selected for the pressure sensor were chosen to allow through-thickness deformability by utilizing a silicone elastomer while having in-plane dimensional stability because of the high modulus aramid fibers. The in-plane stiffness prevents excessive resistance changes due to extensional deformation, ensuring that the sensor response is dominated by out-of-plane pressure. The CNT-aramid-silicone composite sensor has an ultra-wide elastic limit up to 5.8 MPa, which is over 200% and 650% greater than the limits of an aramid-silicone composite without CNTs and a pure silicone, respectively.

The mechanism of resistance change is likely in-plane straining of the piezoresistive network due to the Poisson expansion/dilation of the silicone matrix transferring stress to the fibers in-plane, resulting in an increase in electrical resistance due to elastic strain in the piezoresistive coating. In addition, the sensors have a remarkably wide elastic working range, up to 5.5 ± 0.5 MPa. The sensor shows a repeatable positive pressure correlation with pressure-dependent sensitivity that can be closely linearized in different pressure sensing ranges. The cyclic sensor response has been examined under both displacement- and load-controlled modes in kPa and MPa pressure ranges, displaying good repeatability. Notably, the composite sensor can be utilized to map the spatial distribution of pressure using the EIT technique where local compression increases the sensor resistance (reduced conductivity). Solely relying on boundary measurements, this EIT-based method can cover a large sensing area without any internal wiring and electrodes. Although the electrodes in this research are connected with individual external wires, we envision that, when scaled-up, a flexible circuit board where electrodes are integrated into a

Kapton substrate around the boundary of the sensor would be used. Here, EIT maps demonstrate

accurate estimations for the pressure location, shape and amplitude under single-contact pressure

conditions, but result in larger errors in mapping the pressure shape and amplitude under

multiple-contact pressure conditions. Qualitatively, this pressure mapping methodology has

sufficient spatial and pressure resolution to detect both localized and distributed pressures with

simple contact areas. Future work is aimed at developing advanced EIT algorithms to enhance

pressure-mapping quality.

AUTHOR INFORMATION

Corresponding Author

*E-mail: thosten@udel.edu

Notes

The authors declare no competing financial interest.

ACKNOWLEDGEMENT

The authors gratefully acknowledge the funding support from the National Science Foundation

(Grant 1827729) and the Delaware INBRE program, with a grant from the National Institute of

General Medical Sciences - NIGMS (P20 GM103446) and the state of Delaware.

REFERENCES

[1] Huang Y, Fan X, Chen S, Zhao N. Emerging Technologies of Flexible Pressure Sensors: Materials, Modeling, Devices, and Manufacturing. Advanced Functional Materials

2019;29(12):1808509:1-24.

32

- [2] Zang Y, Zhang F, Di C, Zhu D. Advances of Flexible Pressure Sensors Toward Artificial Intelligence And Health Care Applications. Materials Horizons 2015;2(2):140-156.
- [3] Wang F, Liu S, Shu L, Tao X. Low-Dimensional Carbon Based Sensors and Sensing Network for Wearable Health and Environmental Monitoring. Carbon 2017;121:353-367.
- [4] Wan Y, Wang Y, Guo CF. Recent Progresses on Flexible Tactile Sensors. Materials Today Physics 2017;1:61-73.
- [5] Li J, Bao R, Tao J, Peng Y, Pan C. Recent Progress in Flexible Pressure Sensor Arrays: From Design to Applications. Journal of Materials Chemistry C 2018;6(44):11878-11892.
- [6] Yang T, Xie D, Li Z, Zhu H. Recent Advances in Wearable Tactile Sensors: Materials, Sensing Mechanisms, and Device Performance. Materials Science and Engineering: R: Reports 2017;115:1-37.
- [7] Chun S, Son W, Choi C. Flexible Pressure Sensors Using Highly-Oriented and Free-Standing Carbon Nanotube Sheets. Carbon 2018;139:586-592.
- [8] He Z, Chen W, Liang B, Liu C, Yang L, Lu D, Mo Z, Zhu H, Tang Z, Gui X. Capacitive Pressure Sensor with High Sensitivity and Fast Response to Dynamic Interaction Based on Graphene and Porous Nylon Networks. ACS Applied Materials & Interfaces 2018;10(15):12816-12823.
- [9] Lee B, Kim J, Kim H, Kim C, Lee S. Low-Cost Flexible Pressure Sensor Based on Dielectric Elastomer Film with Micro-Pores. Sensors and Actuators A: Physical 2016;240:103-109.
- [10] Wan S, Bi H, Zhou Y, Xie X, Su S, Yin K, Sun L. Graphene Oxide as High-Performance Dielectric Materials for Capacitive Pressure Sensors. Carbon 2017;114:209-216.
- [11] Hu S, Shi Z, Zhao W, Wang L, Yang G. Multifunctional Piezoelectric Elastomer Composites for Smart Biomedical or Wearable Electronics. Composites Part B: Engineering 2019;160:595-604.
- [12] Wang B, Liu C, Xiao Y, Zhong J, Li W, Cheng Y, Hu B, Huang L, Zhou J. Ultrasensitive Cellular Fluorocarbon Piezoelectret Pressure Sensor for Self-Powered Human Physiological Monitoring. Nano Energy 2017;32:42-49.
- [13] Shi J, Wang L, Dai Z, Zhao L, Du M, Li H, Fang Y. Multiscale Hierarchical Design of a Flexible Piezoresistive Pressure Sensor with High Sensitivity and Wide Linearity Range. Small 2018;14(27):1800819:1-7.
- [14] Park J, Kim J, Hong J, Lee H, Lee Y, Cho S, Kim S, Kim JJ, Kim SY, Ko H. Tailoring Force Sensitivity and Selectivity by Microstructure Engineering of Multidirectional Electronic Skins. NPG Asia Materials 2018;10(4):163-176.
- [15] Liu M, Pu X, Jiang C, Liu T, Huang X, Chen L, Du C, Sun J, Hu W, Wang ZL. Large-Area All-Textile Pressure Sensors for Monitoring Human Motion and Physiological Signals. Adv Mater 2017;29(41):1703700:1-9.
- [16] Chen H, Su Z, Song Y, Cheng X, Chen X, Meng B, Song Z, Chen D, Zhang H.
 Omnidirectional Bending and Pressure Sensor Based on Stretchable CNT PU Sponge.
 Advanced Functional Materials 2017;27(3):1604434:1-9.

- [17] Jian M, Xia K, Wang Q, Yin Z, Wang H, Wang C, Xie H, Zhang M, Zhang Y. Flexible and Highly Sensitive Pressure Sensors Based on Bionic Hierarchical Structures. Advanced Functional Materials 2017;27(9):1606066:1-8.
- [18] Ding Y, Yang J, Tolle CR, Zhu Z. Flexible and Compressible PEDOT: PSS@ Melamine Conductive Sponge Prepared via One-Step Dip Coating as Piezoresistive Pressure Sensor for Human Motion Detection. ACS Applied Materials & Interfaces 2018;10(18):16077-16086.
- [19] Mu C, Song Y, Huang W, Ran A, Sun R, Xie W, Zhang H. Flexible Normal-Tangential Force Sensor with Opposite Resistance Responding for Highly Sensitive Artificial Skin. Advanced Functional Materials 2018;28(18):1707503:1-9.
- [20] Kim K, Hong S, Jang N, Ha S, Lee H, Kim J. Wearable Resistive Pressure Sensor Based on Highly Flexible Carbon Composite Conductors with Irregular Surface Morphology. ACS Applied Materials & Interfaces 2017;9(20):17499-17507.
- [21] Wang L, Peng H, Wang X, Chen X, Yang C, Yang B, Liu J. PDMS/MWCNT-Based Tactile Sensor Array with Coplanar Electrodes for Crosstalk Suppression. Microsystems & Nanoengineering 2016;2:16065:1-8.
- [22] Tewari A, Gandla S, Bohm S, McNeill C, Gupta D. Highly Exfoliated MWNT-rGO Ink-Wrapped Polyurethane Foam for Piezoresistive Pressure Sensor Applications. ACS Applied Materials & Interfaces 2018;10(6):5185-5195.
- [23] Fan F, Lin L, Zhu G, Wu W, Zhang R, Wang ZL. Transparent Triboelectric Nanogenerators And Self-Powered Pressure Sensors Based on Micropatterned Plastic Films. Nano Letters 2012;12(6):3109-3114.
- [24] Dong K, Deng J, Ding W, Wang AC, Wang P, Cheng C, Wang Y, Jin L, Gu B, Sun B. Versatile Core—Sheath Yarn for Sustainable Biomechanical Energy Harvesting and Real-Time Human-Interactive Sensing. Advanced Energy Materials 2018;8(23):1801114:1-12.
- [25] De Volder MF, Tawfick SH, Baughman RH, Hart AJ. Carbon Nanotubes: Present and Future Commercial Applications. Science 2013;339(6119):535-539.
- [26] Doshi SM, Thostenson ET. Thin and Flexible Carbon Nanotube-Based Pressure Sensors with Ultrawide Sensing Range. ACS Sensors 2018;3(7):1276-1282.
- [27] Liu S, Wang L, Feng X, Wang Z, Xu Q, Bai S, Qin Y, Wang ZL. Ultrasensitive 2D ZnO Piezotronic Transistor Array for High Resolution Tactile Imaging. Adv Mater 2017;29(16):1606346:1-6.
- [28] Bao R, Wang C, Dong L, Yu R, Zhao K, Wang ZL, Pan C. Flexible and Controllable Piezo Phototronic Pressure Mapping Sensor Matrix by ZnO NW/p-Polymer LED array. Advanced Functional Materials 2015;25(19):2884-2891.
- [29] Wu S, Peng S, Han ZJ, Zhu H, Wang CH. Ultrasensitive and Stretchable Strain Sensors Based on Mazelike Vertical Graphene Network. ACS Applied Materials & Interfaces 2018;10(42):36312-36322.

- [30] Hao B, Mu L, Ma Q, Yang S, Ma P. Stretchable and Compressible Strain Sensor Based on Carbon Nanotube Foam/Polymer Nanocomposites with Three-Dimensional Networks. Composites Sci Technol 2018;163:162-170.
- [31] Nela L, Tang J, Cao Q, Tulevski G, Han S. Large-Area High-Performance Flexible Pressure Sensor with Carbon Nanotube Active Matrix for Electronic Skin. Nano Letters 2018;18(3):2054-2059.
- [32] Tallman TN, Gungor S, Wang K, Bakis C. Tactile Imaging and Distributed Strain Sensing in Highly Flexible Carbon Nanofiber/Polyurethane Nanocomposites. Carbon 2015:95:485-493.
- [33] Silvera-Tawil D, Rye D, Soleimani M, Velonaki M. Electrical Impedance Tomography for Artificial Sensitive Robotic Skin: A Review. IEEE Sensors Journal 2015;15(4):2001-2016.
- [34] Lee H, Kwon D, Cho H, Park I, Kim J. Soft Nanocomposite Based Multi-Point, Multi-Directional Strain Mapping Sensor Using Anisotropic Electrical Impedance Tomography. Scientific Reports 2017;7:39837:1-10.
- [35] Holder DS. Electrical Impedance Tomography: Methods, History and Applications. Boca Raton: CRC Press, 2004.
- [36] Dai H. An Innovative Sensing Approach Using Carbon Nanotube-Based Composites for Structural Health Monitoring of Concrete Structures. PhD Dissertation, University of Delaware, United States 2017.
- [37] Dai H, Thostenson ET, Schumacher T. Processing and Characterization of a Novel Distributed Strain Sensor Using Carbon Nanotube-Based Nonwoven Composites. Sensors 2015;15(7):17728-17747.
- [38] Dai H, Gallo GJ, Schumacher T, Thostenson ET. A Novel Methodology for Spatial Damage Detection and Imaging Using a Distributed Carbon Nanotube-Based Composite Sensor Combined with Electrical Impedance Tomography. J Nondestr Eval 2016;35(2):1-15.
- [39] Gallo GJ, Thostenson ET. Spatial Damage Detection in Electrically Anisotropic Fiber-Reinforced Composites Using Carbon Nanotube Networks. Composite Structures 2016;141:14-23.
- [40] Vauhkonen M. Electrical Impedance Tomography and Prior Information. PhD Dissertation, University of Kuopio, Finland 1997.
- [41] Polydorides N, Lionheart WR. A Matlab Toolkit for Three-Dimensional Electrical Impedance Tomography: a Contribution to the Electrical Impedance and Diffuse Optical Reconstruction Software Project. Measurement Science and Technology 2002;13(12):1871-1883.
- [42] Vauhkonen PJ, Vauhkonen M, Savolainen T, Kaipio JP. Three-Dimensional Electrical Impedance Tomography Based on the Complete Electrode Model. Biomedical Engineering, IEEE Transactions on 1999;46(9):1150-1160.
- [43] Somersalo E, Cheney M, Isaacson D. Existence and Uniqueness for Electrode Models for Electric Current Computed Tomography. SIAM J Appl Math 1992;52(4):1023-1040.

- [44] Adler A, Guardo R. Electrical Impedance Tomography: Regularized Imaging and Contrast Detection. IEEE Transactions on Medical Imaging 1996;15(2):170-179.
- [45] Graham B, Adler A. Objective Selection of Hyperparameter for EIT. Physiol Meas 2006;27(5):65-79.
- [46] Polydorides N. Image Reconstruction Algorithms for Soft-Field Tomography. PhD Dissertation, University of Manchester Institute of Science and Technology, United Kingdom 2002.
- [47] Karim N, Afroj S, Tan S, Novoselov KS, Yeates SG. All Inkjet-Printed Graphene-Silver Composite Ink on Textiles for Highly Conductive Wearable Electronics Applications. Scientific Reports 2019;9:8035:1-10.
- [48] Sarker F, Potluri P, Afroj S, Koncherry V, Novoselov KS, Karim N. Ultrahigh Performance of Nanoengineered Graphene-Based Natural Jute Fiber Composites. ACS Applied Materials & Interfaces 2019;11(23):21166-21176.
- [49] Zheng Y, Li Y, Li Z, Wang Y, Dai K, Zheng G, Liu C, Shen C. The Effect of Filler Dimensionality on the Electromechanical Performance of Polydimethylsiloxane Based Conductive Nanocomposites for Flexible Strain Sensors. Composites Sci Technol 2017;139:64-73.
- [50] Zheng Y, Li Y, Dai K, Wang Y, Zheng G, Liu C, Shen C. A Highly Stretchable and Stable Strain Sensor Based on Hybrid Carbon Nanofillers/Polydimethylsiloxane Conductive Composites for Large Human Motions Monitoring. Composites Sci Technol 2018;156:276-286.
- [51] Razak AHA, Zayegh A, Begg R, Wahab Y. Foot Plantar Pressure Measurement System: a Review. Sensors 2012;12:9884-9912.
- [52] Lee W, Yeo K, Andriyana A, Shee Y, Adikan FM. Effect of Cyclic Compression and Curing Agent Concentration on the Stabilization of Mechanical Properties of PDMS Elastomer. Mater Des 2016;96:470-475.
- [53] Wang L, Wang X, Li Y. Relation between Repeated Uniaxial Compressive Pressure and Electrical Resistance of Carbon Nanotube Filled Silicone Rubber Composites. Composites Part A: Applied Science and Manufacturing 2012;43(2):268-274.
- [54] Gonçalves B, Oliveira J, Costa P, Correia V, Martins P, Botelho G, Lanceros-Mendez S. Development of Water-Based Printable Piezoresistive Sensors for Large Strain Applications. Composites Part B: Engineering 2017;112:344-352.
- [55] Wu X, Lu C, Han Y, Zhou Z, Yuan G, Zhang X. Cellulose Nanowhisker Modulated 3D Hierarchical Conductive Structure of Carbon Black/Natural Rubber Nanocomposites for Liquid and Strain Sensing Application. Composites Sci Technol 2016;124:44-51.

For Table of Contents Only

